Research Square

Preprints are preliminary reports that have not undergone peer review.
They should not be considered conclusive, used to inform clinical practice,
or referenced by the media as validated information.

Statistical evidence for the Mediterranean response to the 2012 North Atlantic great salinity anomaly

Gian Luca Eusebi Borzelli

luca_borzelli@yahoo.it

Center for Remote Sensing of the Earth - CeRSE

Sandro Carniel

CNR, Istituto di Scienze Polari

Ernesto Napolitano

ENEA-SSP-CLIMAR-MSC

Cosimo Enrico Carniel

ETH Zurich

Mauro Sclavo

CNR, Istituto di Scienze Polari

Article

Keywords:

Posted Date: July 23rd, 2026

DOI: https://doi.org/10.21203/rs.3.rs-9986247/v1

License: This work is licensed under a Creative Commons Attribution 4.0 International License.
Read Full License

Additional Declarations: No competing interests reported.

Statistical evidence for the Mediterranean response to the 2012 North Atlantic great salinity anomaly

by

Gian Luca Eusebi Borzelli[(1*)], Sandro Carniel[(2)], Ernesto Napolitano[(3)], Cosimo Enrico Carniel[(4)]
Mauro Sclavo[(2)]

[(1)]Center for Remote Sensing of the Earth (CeRSE), Rome Italy. e-mail: luca_borzelli@yahoo.it; gianluca.borzelli@cerse.it

[(2)]CNR, Istituto di Scienze Polari, Venezia Italy.

[(3)]ENEA-SSP-CLIMAR-MSC, Via Anguillarese 301, Rome Italy

[(4)]Institute for Atmospheric and Climate Sciences, ETH Zürich, Zurich, Switzerland.

[(*)]Corresponding author

Abstract

In 2012, the subpolar North Atlantic experienced an unprecedented influx of freshwater, resulting in significantly reduced salinity levels. This event, known as the Great Salinity Anomaly (GSA), was widespread and propagated to the mid-latitudes of the North Atlantic. In this study, we provide statistical evidence of the GSA impact on the Mediterranean sea surface and thermohaline structure. Our findings indicate that the GSA remained active in the North Atlantic until mid-2023 and affected the Mediterranean until 2024. This was primarily due to a decrease in salinity of Atlantic water in the southwestern Mediterranean (SWMED), resulting in an increase in halosteric sea level. Additionally, we show that, overall, thermosteric effects, primarily driven by global warming, have a greater influence on changes in sea surface height (SSH) at the basin scale in the Mediterranean, with the exception of the SWMED where both thermosteric and halosteric effects contribute equally to the SSH increase.

1. Introduction

In the years 2012-2016, the subpolar North Atlantic (SPNA see Figure S1a in the supplementary material) experienced a significant freshwater pulse, resulting in extremely low salinity levels. This was caused by an increase in Arctic freshwater release and was carried by ocean currents [1,2]. This event was widespread, with strong freshening observed throughout the entire SPNA, reaching as far as the mid latitudes and affecting waters from the surface down to a depth of 1000 m [2]. These large-scale freshening events in the SPNA are known as great salinity anomalies (GSAs) and are recurrent occurrences of widespread freshening in the North Atlantic. They are believed to be linked to an intensification of the subpolar gyre [3,4], whose strength is influenced by an enhanced North Atlantic Oscillation (NAO) [5]. This leads to an increased flow of freshwater from the East Greenland Current into the Labrador Sea during the melting season [1,6]. Notable GSAs have occurred in the 1970s, 1980s, and 1990s [7,8], but the event in 2012 was the most significant in the last 120 years [2].

The Mediterranean Sea is a semi-enclosed basin in the mid-latitudes, connected to the Atlantic Ocean through the Strait of Gibraltar (see Figure S1b in supplementary material). It is divided into two main sub-basins, the Western Mediterranean (WMED) and the Eastern Mediterranean (EMED), which are connected by the Channel of Sicily. The surface circulation of the basin is described as an open thermohaline cell: Atlantic waters (AWs) enter the WMED through the Strait of Gibraltar and travel eastward along the North African coast before entering the EMED through the Channel of Sicily [9,10]. In the easternmost part of the EMED, surface AW is transformed into Levantine intermediate water (LIW), one of the saltiest water masses, through air-sea heat and moisture fluxes. Therefore, the EMED is a concentration basin. Variability in salinity at the sub-basin scale has been attributed to oceanic effects on interannual-to-decadal timescales [11,12], while long-term changes in the NAO influence the Mediterranean water balance [13,14].

In the SPNA, a positive NAO phase generally leads to lower sea surface salinity (SSS), while in the Mediterranean, particularly in the EMED, a positive NAO phase leads to higher SSS due to increased evaporation and reduced precipitation [15,16]. In this study, we demonstrate that: i) the GSA in the SPNA, which began at the end of 2010, remained active until the middle of 2023; ii) starting in early 2012, the water entering the WMED from the Atlantic and flowing along the North African coast became fresher than normal, resulting in a regional increase in the halosteric sea level; iii) the spatial patterns of the anomaly of the salinity averaged between 0 and 150 m in the WMED were highly correlated with the spatial pattern of the SSS anomaly in the SPNA, with a delay of approximately 13 months; iv) when comparing halosteric and thermosteric sea level changes, thermosteric effects dominate over halosteric effects in determining sea level changes throughout the Mediterranean, except in the WMED along the North African region, where the two components have a similar effect on changes in the sea surface structure.

2. Results and Discussion

Figure 1 shows the leading Empirical Orthogonal Functions (EOFs) for the average salinity from the surface to a depth of 150 m (SSS) separately calculated for the SPNA (Figure 1a) and the Mediterranean Sea (Figure 1b). In the SPNA, EOF1 exhibits a large-scale pattern of negative anomalies centered over the central subpolar gyre, representing the dominant mode of interannual freshening. The corresponding Principal Component (PC, Figure 1c, blue line) shows a significant decrease in SSS starting in late 2010, reaching its peak around 2017, and gradually dissipating by 2023, in line with the GSA described by Holliday et al. [2].

In the Mediterranean, EOF1 exhibits a more complex spatial structure. In the WMED, negative anomalies are confined along the North African coast, in the region typically occupied by AW, while positive anomalies dominate the northern WMED and most of the EMED. The associated PC (Figure 1c, red line) indicates a long-term increase in Mediterranean SSS, in agreement with previous studies [13-15], with the notable exception of a freshening signal along the African coast emerging after 2012.

Interestingly, a lead-and-lag analysis between the red and blue lines in Figure 1c (Figure 1d) reveals that the leading PCs of the SSS in the SPNA and the Mediterranean are lagged by 13 months, with the SPNA leading and a high correlation coefficient of 0.83. This result suggests that the freshening of Atlantic Water in the Mediterranean can be statistically linked to the GSA, with a characteristic delay of about one year. To test the dynamical causality between freshening of Atlantic Water in the Mediterranean and the GSA, we used the Convergent Cross Mapping (CCM) method to reconstruct the leading PC of the SSS in the SPNA from the leading PC of the SSS in the Mediterranean. Figure 1e compares the original and the CCM-reconstructed PC obtained with E =12, and τ=4. Although CCM does not allow to reconstruct the PC prior to date $t[(E-1)\cdot\tau+1]$ = 01-Sep-1996, over the subsequent period the original and reconstructed PC are very similar. This indicates that, from the statistical perspective, PC1 of the salinity field in the North Atlantic and in the Mediterranean are related by a causal relationship, at least over the period Oct-1996 until Dec-2024.

To further investigate the linkage between the freshening of AW in the Mediterranean and the GSA, we applied Singular Value Decomposition (SVD) to the 13-month lagged covariance between SPNA and Mediterranean SSS fields. The leading SVD mode explains 87% of the total covariance and displays a coherent pattern connecting the GSA-related freshening in the SPNA (Figure 2a) with negative salinity anomalies along the North African coast in the Mediterranean (Figure 2b). The corresponding PCs (blue and red line in Figure 2c) are significantly correlated, with the SPNA leading of approximately 12 months (r = 0.87, see Figure S2 in the supplementary material). Furthermore, the time series presented in Figure 2c are nearly perfectly anti-correlated with the leading PCs of the EOF analysis (Figure 1c) performed over the SPNA (r=-0.96) and the Mediterranean (r=-0.98). This indicates that freshening of Mediterranean AW covaries with freshening in the SPNA due to the GSA.

To evaluate the impact of salinity changes resulting from the GSA on Mediterranean SSH and compare it to the effects of temperature, we analyzed the variability in sea level caused by both halosteric and thermosteric components. Figure 3a illustrates the leading mode of the SVD between halosteric levels and SSH, while Figure 3b displays the leading mode of the SVD between thermosteric levels and SSH. In Figure 3a, three distinct regions can be observed. The first, located over the Algerian basin and typically occupied by Atlantic water, is characterized by high positive values. The second region, in the Liguro-Provencal-Catalan basin, is characterized by negative values, and the third region, covering most of the EMED, also shows negative values. Overall, this mode describes the competing effects of salinification due to enhanced evaporation from global warming [17] and freshening of AW associated with the GSA on the Mediterranean SSH. The temporal variability of the covariance mode between halosteric sea level and SSH is represented by the corresponding PC of the SVD, as shown in Figure 3c. Prior to approximately 2012, this mode exhibits oscillations around zero. However, after 2012, the amplitude of this mode gradually increases. This suggests that the competing effects of Mediterranean surface water salinification and freshening of AW on the SSH began in 2012.

Furthermore, our data shows that this process continued even after the GSA ended in 2023, as evidenced by the continued increase in the PC until 2024. In general, we can affirm that the first mode of co-variability between halosteric levels and SSH describes an increase in halosteric sea level along the path of AW up to the Strait of Sicily, starting from 2012. In contrast, in the northern WMED and EMED, halosteric effects result in a decrease in sea level. This is consistent with the findings of Grodsky et al. [16], who reported a steady salinification of the EMED at a rate of approximately 0.14 psu/year during 2015–2018.

The analysis of sea level variability due to thermosteric effects is also noteworthy, as these effects have different impacts on the Sea Surface Height (SSH) in the EMED and WMED. Figure 3b shows that changes in SSH associated with thermosteric effects are primarily concentrated in the EMED, while these effects are relatively weak in the WMED. Additionally, the temporal variability of SSH induced by thermosteric effects, as revealed by the projection of the thermosteric levels time series over the leading mode of the SVD between SSH and thermosteric levels, shows a steady increasing trend throughout the entire observation period (Figure 3d).

One important factor to consider is the relative importance of thermosteric and halosteric effects, particularly those associated with the GSA, in determining changes in Mediterranean Sea SSH. In order to investigate this issue, we used the linear model described in equation (8) to represent standardized SSH anomaly data obtained from altimeters. As mentioned in paragraph 2.4, the square of the coefficients a_T and a_S represent the fractions of variance of the overall SSH anomaly variance explained by thermosteric and halosteric effects, assuming weak correlations between the variables

that contribute to changes in the SSH. Figure 4a shows the square of a_S, while Figure 4b shows the square of a_T. In Figures S3a and S3b of the supplementary material, we show the p-value of a_S and a_T. Comparing Figures 4a and 4b we see that thermosteric levels dominate on halosteric nearly everywhere in the Mediterranean except that along the north African coast, in the region occupied by AW, where halosteric effects are stronger than thermosteric in determining changes of the SSH. We therefore conclude that salinity changes in the SPNA determine important changes in the Mediterranean SSH in the southwestern Mediterranean.

3. Conclusion

In our study, we examined the impact of the GSA that originated in the SPNA around 2011-2012 [2] on the Mediterranean Sea. Our findings suggest that the source of fresh water in the SPNA remained active until mid-2023. We also found statistical evidence of a causal relationship between changes in SSS in the SPNA and SSS changes of Atlantic water entering the Mediterranean. This statistical analysis indicates that the GSA affected the Mediterranean thermohaline structure until the end of 2024, primarily through a gradual freshening of Atlantic water in the southwestern part of the basin. This resulted in an increase in the halosteric effects in the Algerian basin, which, unlike the rest of the Mediterranean, were comparable to the thermosteric effect. However, it is important to note that our results are based on statistical analysis rather than deterministic flow-tracking techniques. To conclusively address the causal relationship between GSA and changes in the Mediterranean Sea surface and thermohaline structure, further research is necessary to specifically track salt flows from the Atlantic into the Mediterranean.

4. Data and Methods

4.1 The data

The data used in this study includes temperature, salinity (TS), and SSH data from the Copernicus data archive of the European Union. This archive provides global TS data on a daily and monthly basis, covering the water column from the surface down to 5500 m over 50 vertical levels. The data is regularly sampled over a spatial grid of 1/8º×1/8º and covers the period from 1 January 1993 to the present (data set ARMOR3D L4, see [18]). Global SSH data (data set Global Ocean Gridded L 4 Sea Surface Heights and derived variables, see [19]) is available on a daily basis with a spatial resolution of 1/8º×1/8º and covers the same time period as the TS data. From these data sets, the subsets covering regions 45ºN-65ºN, 55ºW-5ºW (the SPNA) and 30ºN-45ºN, 5ºW-35ºE (the Mediterranean) over the period January 1993-December 2024 were extracted. Due to the specific morphology of the Gibraltar Strait, only Atlantic waters that are located above 150 m can enter the Mediterranean. As a result, our analysis was limited to TS data from the surface and a depth of 150 m. Therefore, with SSS it is intended the salinity averaged over the first 150 m of the water column. SSH data was interpolated

on a monthly basis. Anomalies were calculated for all variables discussed in this study, using the period of 1993-2022 as the reference climatological baseline.

4.2 Estimation of the SPNA-Mediterranean salinity covariance

To determine the level of covariance between the SSS anomaly in the SPNA and the Mediterranean, we first calculated the depth-averaged salinity from 0 to 150 m in both basins. Next, we computed the anomalies, as discussed in the previous paragraph. To further analyze the data, we conducted an EOF analysis and a SVD analysis on the two fields. To begin, we performed the dimensionless EOF analysis of the SSS separately in the two basins as prescribed in [20]. This allowed us to identify the main patterns of SSS variability, described by the leading EOFs, and their temporal variability, described by the corresponding PCs. We then conducted a lead-and-lag analysis between the first PC of the SSS in the two basins to identify any delays between the signals and determine their level of correlation. Finally, we analyzed the covariance between the SSS in the SPNA and in the Mediterranean using the SVD of the covariance matrix at lag Δ deduced from the lead-and-lag analysis between the first PCs of the two basins.

To briefly review the SVD technique we closely follow the formalism and definitions of Bretherton et al. [21]. We denote the SSS fields at date t_j ($j = 1...J$) over the Mediterranean and the SPNA, as $f(x_l,t_j)$ and $g(y_m,t_j)$ respectively. The SSS in the Mediterranean at any given date is determined by a set of L observations at points x_l ($l = 1...L$), while the SSS over the SPNA is defined by a set of M observations at points y_m ($m = 1...M$). The SVD technique identifies the patterns of maximum covariance between the fields f and g. To do this, we define the data matrices $(\boldsymbol{F})_{lj} = f(x_l,t_j)$ and $(\boldsymbol{G})_{mj} = g(y_m,t_j)$ and use them to create a delayed covariance matrix of the SSS between the Mediterranean and SPNA at a lag of $\Delta = (a-1)\cdot\delta$, with δ being the sampling interval, and a an integer positive number that defines the delay, i.e.

$$(\boldsymbol{K})_{lm} = \frac{1}{J-a-1}\cdot\sum_{j=1}^{J-a} f\left(x_l, t_{j+a}\right) g\left(y_m, t_j\right) \tag{1}$$

Note that the matrix $\boldsymbol{K}$ is, in general, a rectangular $L\times M$ matrix and diagonalization requires SVD technique (see e.g. [22]). Specifically, SVD consists in the factorizing the matrix $\boldsymbol{K}$ as

$$\boldsymbol{K} = \boldsymbol{USV}^T \tag{2}$$

where $\boldsymbol{U}$ is an $L\times M$ unitary matrix, $\boldsymbol{S}$ is a diagonal $M\times M$ matrix that contains the eigenvalues of $\boldsymbol{K}$ (also known as singular values), and $\boldsymbol{V}$ is an $M\times M$ unitary matrix with the suffix T indicating transposition. The columns of $\boldsymbol{U}$ contain the left eigenvectors of $\boldsymbol{K}$, which represent the spatial structures in the Mediterranean that define the SSS patterns that occur to achieve maximum correlation with the SPNA. On the other hand, the columns of $\boldsymbol{V}$ represent the right eigenvectors of

$\boldsymbol{K}$, which describe the coupled spatial patterns over the SPNA. The pairs of left and right eigenvectors of $\boldsymbol{K}$ define the coupled spatial distributions of the SSS signal and illustrate how SSS changes manifest simultaneously across both regions when their covariance is maximized. In this formalism, the singular values define the maximum achievable covariance for each pair of left and right eigenvectors, and their squared values represent the total covariance captured by that pair. The PCs of the SVD are defined as the projections of the original data onto the respective eigenvectors and represent the temporal evolution of the coupled covariance of the SSS field in the Mediterranean and SPNA.

4.3 Statistical causality between the salinity changes in the Mediterranean and the North Atlantic: Convergent Cross Mapping technique.

In dynamical systems, causality is defined by the influence of a source variable (X) on a sink variable (Y). If X causes *Y,* then Y is not independent; rather, information about the states of X are embedded in *Y.* Consequently, we can use historical values of Y to reconstruct the states of *X.* The properties of such a system are fully captured by its system manifold M, a hypersurface in phase-space describing the mutual variability of the system variables. Unless the underlying dynamics are known, M remains unknown, and we must rely on "snapshots" of the dynamics derived from observations. Following Takens' embedding theorem [23], the time series *X(t)* and *Y(t)* can be used to generate "shadow manifolds" (M_x and M_y) of the system manifold. To construct these shadow manifolds, it is necessary to define the embedding dimension E. This parameter represents the number of independent variables necessary to unfold the system's dynamics. According to Takens' theorem, if the original system manifold has a dimension d, an embedding dimension of E>2d is sufficient to ensure that the shadow manifold M_y is a faithful representation of the system manifold. In practice, the basic idea of the CCM [24,25] method consists in generating a library of shadow manifold vectors $\boldsymbol{y}(t)$ from the time series *Y(t)* using the embedding dimension E and time lag τ, i.e.

$$\boldsymbol{y}(t) = [Y(t), Y(t-\tau), Y(t-2\cdot\tau), \ldots, Y(t-(E-1)\cdot\tau)] \quad (3)$$

This vector represents a point in the shadow manifold M_y. To estimate a state of X at time t (denoted as $\hat{X}(t)$) using the manifold M_y, we first identify the $E+1$ nearest neighbors of the point $\boldsymbol{y}(t)$ in the shadow manifold. The distances between the current point $\boldsymbol{y}(t)$ and its j^{th} neighbor are calculated as:

$$d_j = \|\boldsymbol{y}(t) - \boldsymbol{y}(t_j)\| \quad (4)$$

where the double vertical line indicates the Euclidean distance and t_j are the time indices of the $E+1$ closest neighboring points. Once the $E+1$ closest neighboring points are identified, the estimate of X at time t is

$$\hat{X}(t) = \sum_{j=1}^{E+1} w_j \, X(t_j) \tag{5}$$

where w_j are weights defined as

$$w_j = exp\left(-d_j / min\left\{d_i\right\}_{\{i=1\ldots E+1\}}\right) \tag{6}$$

The "strength" of the causal link between X and Y is determined by the Pearson correlation coefficient between the actual values of $X(t)$ and the reconstructed values $\hat{X}(t)$.

In this research, we have used the CCM algorithm available at https://it.mathworks.com/matlabcentral/fileexchange/52964-convergent-cross-mapping by setting the cause variable X equal to the leading PC of the EOF analysis of the SSS over the SPNA, and the sink variable Y, the leading PC of the EOF analysis of the SSS over the Mediterranean.

4.4 Estimation of halosteric and thermosteric sea level changes

Following Jayne et al. [26] changes in sea level caused by thermosteric (η_{th}) and halosteric (η_{ha}) effects in the region of the water column between the surface and a depth D are given by

$$\eta_{th}(x,y,t) = \int_{-D}^{0} dz \, \alpha(x,y,z,t) \cdot T'(x,y,z,t) \tag{7a}$$

$$\eta_{ha}(x,y,t) = -\int_{-D}^{0} dz \, \beta(x,y,z,t) \cdot S'(x,y,z,t) \tag{7b}$$

In equations (7a) and (7b) T' indicates the temperature fluctuation about its depth averaged value, S' the salinity fluctuation about its depth averaged value, and α and β represent the thermal expansion and haline contraction coefficients.

In this analysis, we chose to focus on the region of the water column between 0 and 150 m because this is where the AW is typically found in the Mediterranean.

4.5 Linear model between sea surface high, halosteric and thermosteric levels

To determine the relative impact of thermosteric and halosteric effects on changes in sea surface height (SSH), we utilized a linear model that links standardized SSHs with standardized thermosteric and halosteric deformations of the sea surface. This can be represented as follows:

$$\eta'(x,y,t) = a_T(x,y,t) \cdot \eta'_{th} + a_S(x,y,t) \cdot \eta'_{ha} + R(x,y,t) \quad (8)$$

Where the prime symbol indicates standardization of the respective variable, while R encompasses all other factors that may contribute to changes in SSH, aside from halosteric and thermosteric effects. Note that, using this formalism and assuming weak correlations between the different variables on the right-hand side of equation (8), a_T^2 and a_S^2 actually represent the fraction of variance of the overall SSH variance explained by thermosteric and halosteric effects.

To estimate the coefficients $\underline{a_T}$ and a_S we minimized the least square between measured SSHs and their representations in terms of thermosteric and halosteric sea surface high.

Data Availability

Data used in this research can be downloaded succumbing to European Union (EU) regulations on geophysical data exchange (see https://www.copernicus.eu/en/international-cooperation-area-data-exchange).

Original TS data can be downloaded from the Copernicus data archive by registered users at
https://doi.org/10.48670/moi-00052
while original SSH data are available to registered users at
https://doi.org/10.48670/moi-00148

Code Availability

Codes used in this research are available upon reasonable request.

References

[1] Tesdal, J. E., Abernathey, R. P., Goes, J. I., Gordon, A. L., & Haine, T. W. (2018). Salinity trends within the upper layers of the subpolar North Atlantic, *Journal of Climate*, **31**(7), 2675-2698. doi: 10.1175/JCLI-D-17-0532.1

[2] Holliday, N. P., Bersch, M., Berx, B., Chafik, L., Cunningham, S., Florindo-López, C., et al. (2020). Ocean circulation causes the largest freshening event for 120 years in eastern subpolar North Atlantic. *Nature communications*, **11**(1), 585. doi: 10.1038/s41467-020-14474-y

[3] Lankhorst, M., and Send, U. (2020). Uncertainty of North Atlantic current observations from altimetry, floats, moorings, and XBT. *Progress in Oceanography*, **187**, 102402. doi: 10.1016/j.pocean.2020.102402

[4] Tesdal, J.-E., and Haine, T. W. N. (2020). Dominant terms in the freshwater and heat budgets of the Subpolar North Atlantic Ocean and Nordic Seas from 1992 to 2015. *Journal of Geophysical Research: Oceans*, **125**, e2020JC016435. doi: 10.1029/2020JC016435

[5] Häkkinen, S., Rhines, P. (2004). Decline of Subpolar North Atlantic circulation during the 1990s. *Science*, **304**(5670), 555–559. doi: 10.1126/science.1094917

[6] Hu, R., and Zhao, J. (2022). Sea surface salinity variability in the western subpolar North Atlantic based on satellite observations. *Remote Sensing of Environment*, **281**, 113257. doi: 10.1016/j.rse.2022.113257

[7] Belkin, I. M., Levitus, S., Antonov, J., Malmberg, S. A. (1998). "Great salinity anomalies" in the North Atlantic, *Progress in Oceanography*, **41**(1), 1-68. doi: 10.1016/S0079-6611(98)00015-9

[8] Belkin, I. M. (2004). Propagation of the "Great Salinity Anomaly" of the 1990s around the northern North Atlantic, *Geophysical Research Letters*, **31**(8). doi: 10.1029/2003GL019334

[9] Malanotte-Rizzoli, P., Artale, V., Eusebi Borzelli, G. L., Brenner, S., Crise, A., Gačić, M., et al. (2014). Physical forcing and physical/biochemical variability of the Mediterranean Sea: a review of unresolved issues and directions for future research. *Ocean Science*, **10**(3), 281-322. doi: 10.5194/os-10-281-2014

[10] Vargas-Yáñez, M., Ouradou, M., Moya, F., Ballesteros, E., Alonso, C., Serra, M., et al... & Hernández-Guerra, A. (2025). A time series of water mass transports through the Balearic Channels using an ocean circulation inverse method: 1996–2022. *Progress in Oceanography*, 103525. doi: 10.1016/j.pocean.2025.103525

[11] Gačić, M., Civitarese, G., Eusebi Borzelli, G. L., Kovačević, V., Poulain, P. M., Theocharis, A., et al. (2011). On the relationship between the decadal oscillations of the northern Ionian Sea and the salinity distributions in the eastern Mediterranean. *Journal of Geophysical Research: Oceans*, **116**(C12). doi:10.1029/2011JC007280

[12] Gačić, M., Schroeder, K., Civitarese, G., Cosoli, S., Vetrano, A., Eusebi Borzelli, G. L. (2013). Salinity in the Sicily Channel corroborates the role of the Adriatic–Ionian Bimodal Oscillating System (BiOS) in shaping the decadal variability of the Mediterranean overturning circulation. *Ocean Science*, **9**(1), 83-90. doi: 10.5194/os-9-83-2013

[13] Tsimplis, M.N., Josey, S.A. (2001) Forcing of the Mediterranean Sea by atmospheric oscillations over the North Atlantic. *Geophysical Research Letters*, **28**, 803–806. doi: 10.1029/2000GL012098

[14] Mariotti, A. (2010). Recent changes in the Mediterranean water cycle: a pathway toward long-term regional hydroclimatic change? *Journal of Climate*, **23**, 1513–1525. doi: 10.1175/2009JCLI3251.1

[15] Tsimplis, M. N., Calafat, F. M., Marcos, M., Jordá, G., Gomis, D., Fenoglio-Marc, L., et al. (2013). The effect of the NAO on sea level and on mass changes in the Mediterranean Sea. *Journal of Geophysical Research: Oceans*, **118**(2), 944-952. doi: 10.1002/jgrc.20078

[16] Grodsky, S. A., Reul, N., Bentamy, A., Vandemark, D., Guimbard, S. (2019). Eastern Mediterranean salinification observed in satellite salinity from SMAP mission. *Journal of Marine Systems*, **198**, 103190. doi: 10.1016/j.jmarsys.2019.103190

[17] Skliris, N., Marsh, R., Breedon, M., Josey, S. A. (2024). Accelerated warming and salinification of the Mediterranean Sea: Implications for dense water formation. *Journal of Marine Science and Engineering*, **13**(1), 25.

[18] Buongiorno Nardelli, B. (2020). A Multi-Year Timeseries of Observation-Based 3D Horizontal and Vertical Quasi-Geostrophic Global Ocean Currents. *Earth System Science Data*, **12**, 1711–1723. doi: 10.5194/essd-12-1711-2020

[19] Pujol, M.-I., Grassi, K. (2025). *Product User Manual for Sea Level Altimeter Products, Issue 1*. European Commission-EU Copernicus Marine Service. doi: 10.48670/moi-00148

[20] Eusebi Borzelli, G. L., Carniel, S., Carniel, C. E., Russo, A. (2024). The Atlantic Niño mode: a thermodynamic or a dynamic phenomenon?. *Journal of Geophysical Research: Oceans*, **129**(6), e2024JC021067. doi: 10.1029/2024JC021067

[21] Bretherton, C. S., Smith, C., Wallace, J. M. (1992). An intercomparison of methods for finding coupled patterns in climate data. *Journal of Climate*, **5**(6), 541-560. doi: 10.1175/1520-0442(1992)005<0541:AIOMFF>2.0.CO;2

[22] Banerjee, S., Roy, A. (2014). *Linear Algebra and Matrix Analysis for Statistics.* Texts in Statistical Science (1st ed.). Chapman and Hall/CRC. ISBN 978-1-4200-9538-8.

[23] Takens, F. (1981). Detecting strange attractors in turbulence, in *Dynamical Systems and Turbulence*, Warwick 1980 (Lecture Notes in Mathematics, Vol. 898, pp. 366-381). Springer, Berlin, Heidelberg.

[24] Sugihara, G., May, R., Ye, H., Hsieh, C.-H., Deyle, E., Fogarty, M., Munch, S. (2012). Detecting causality in complex ecosystems, *Science*, **338**, 496-500. doi: 10.1126/science.1227079

[25] Tsonis A.A., Deyle E.R., Ye H., Sugihara G. (2018). Convergent Cross Mapping: Theory and an Example. In: Tsonis A. (eds) *Advances in Nonlinear Geosciences*. Springer, Cham. doi: 10.1007/978-3-319-58895-7_27

[26] Jayne, S. R., Wahr, J. M., Bryan, F. O. (2003). Observing ocean heat content using satellite gravity and altimetry. *Journal of Geophysical Research: Oceans*, **108**(C2). doi: 10.1029/2002JC001619

Funding

The authors declare that no direct funding, grants, or financial support from any public, commercial, or non-profit sector was received for the research, authorship, and/or publication of this article.

Author Contributions

All the authors contributed equally to the work. G.L.E.B. and S.C. proposed the original idea. G.L.E.B and E.N. designed the research. All authors contributed to analyze the data and to interpret the results. G.L.E.B. and C.E.C. provided the figures. G.L.E.B. wrote the initial version of the manuscript, S.C., E.N., C.E.C. and M.S. provided corrections and comments.

Competing Interests

The authors declare no competing interest.

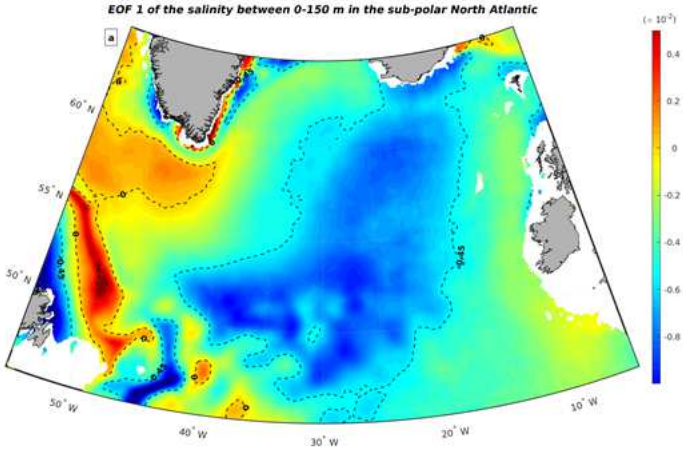
Caption to Figures

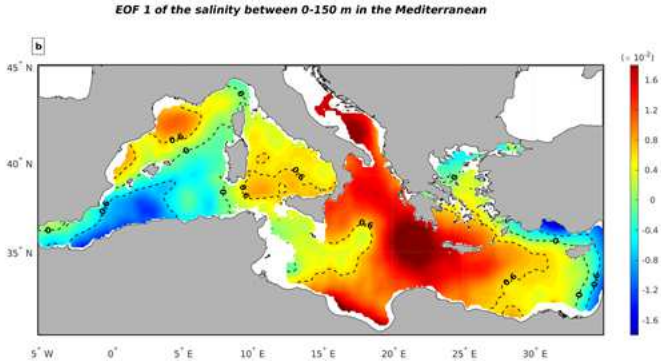
Figure 1: EOF analysis of the SSS in the SPNA and in the Mediterranean and lead-and-lag analysis between leading PCs. a) EOF1 in the SPNA; b) EOF1 in the Mediterranean; c) PC1 in the SPNA (blue line) and in the Mediterranean (red line); d) lead-and-lag analysis between PC1 in the SPNA and Mediterranean; e) leading PC of the salinity in the North Atlantic (red line) and the same PC reconstructed from the PC1 of the salinity in the Mediterranean using the CCM method (blue line)

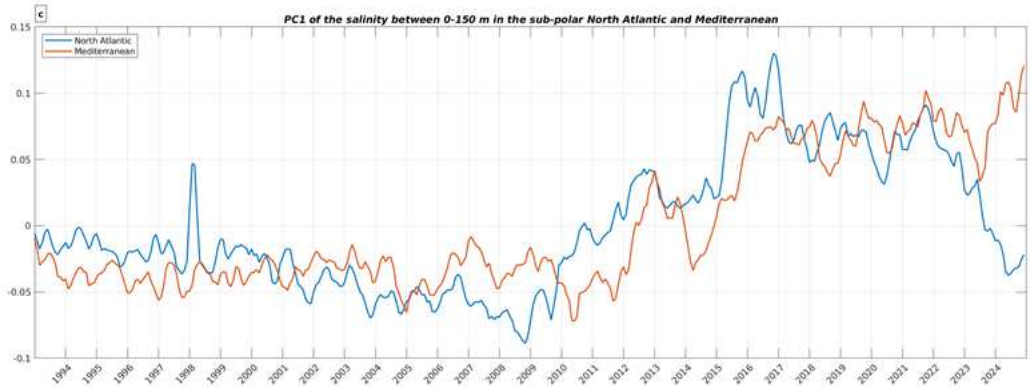
Figure 2: SVD of the SSS covariance matrix between Mediterranean and SPNA. a) Leading right eigenvector (SPNA) of the covariance matrix; b) leading left eigenvector (Mediterranean) of the covariance matric; c) SVD PCs of the right (blue line, SPNA) and left (red line, Mediterranean) leading eigenvectors.

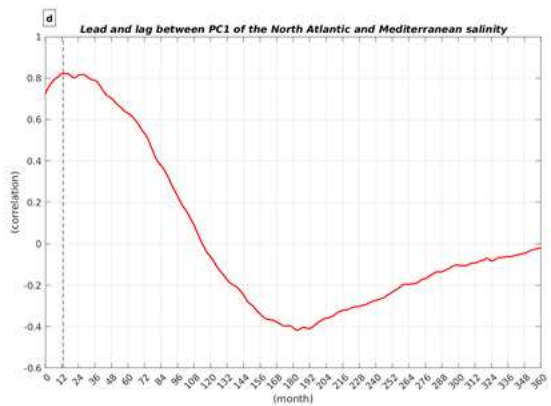
Figure 3: SVD of halosteric level-SSH covariance matrix and thermosteric level-SSH covariance matrix. a) Leading (left) eigenvector of the halosteric level-SSH covariance matrix; b) leading (left) eigenvector of thermosteric level-SSH covariance matrix; c) PC of the leading eigenvector of the halosteric level-SSH covariance matrix; d) PC of the leading eigenvector of the thermosteric level-SSH covariance matrix.

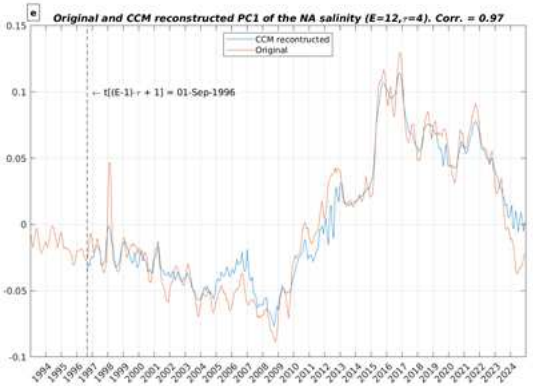
Figure 4: a) Percentage of the SSH anomaly variance explained by halosteric sea level changes (i.e. $100 \times a_s^2$); b) Percentage of the SSH anomaly variance explained by thermosteric sea level changes (i.e. $100 \times a_T^2$).

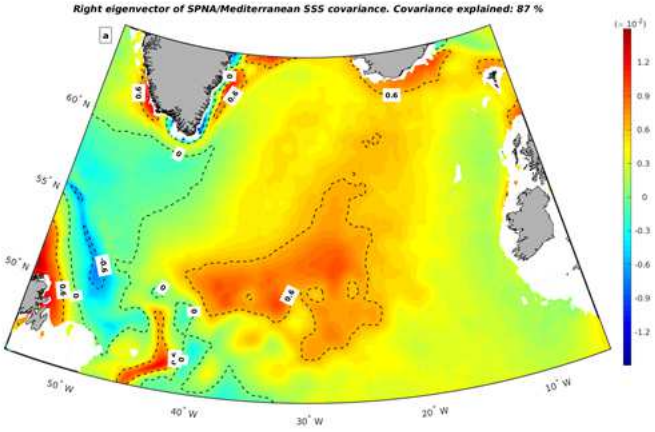

a
EOF 1 of the salinity between 0-150 m in the sub-polar North Atlantic
(× 10⁻²)
0.4
0.2
0
-0.2
-0.4
-0.6
-0.8
60° N
55° N
50° N
50° W
40° W
30° W
20° W
10° W

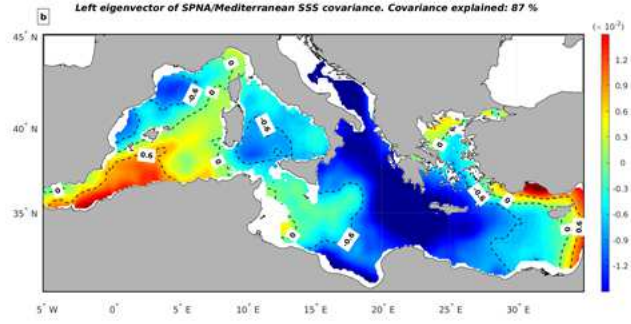

b
EOF 1 of the salinity between 0-150 m in the Mediterranean
(× 10⁻²)
1.6
1.2
0.8
0.4
0
-0.4
-0.8
-1.2
-1.6
45° N
40° N
35° N
5° W
0°
5° E
10° E
15° E
20° E
25° E
30° E

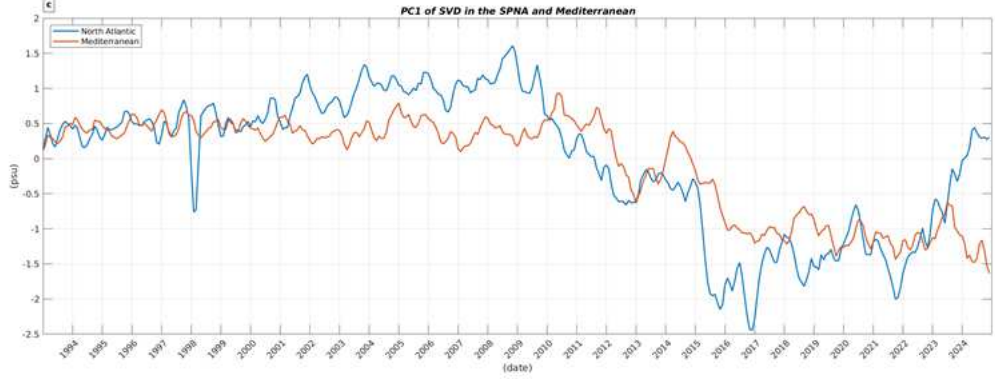

c
PC1 of the salinity between 0-150 m in the sub-polar North Atlantic and Mediterranean
North Atlantic
Mediterranean
0.15
0.1
0.05
0
-0.05
-0.1
1994
1995
1996
1997
1998
1999
2000
2001
2002
2003
2004
2005
2006
2007
2008
2009
2010
2011
2012
2013
2014
2015
2016
2017
2018
2019
2020
2021
2022
2023
2024

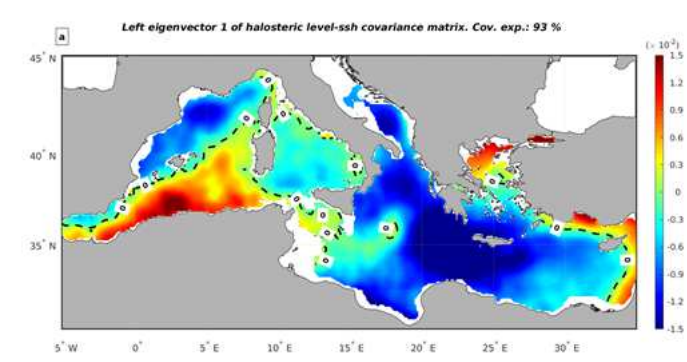

d
Lead and lag between PC1 of the North Atlantic and Mediterranean salinity
(correlation)
(month)

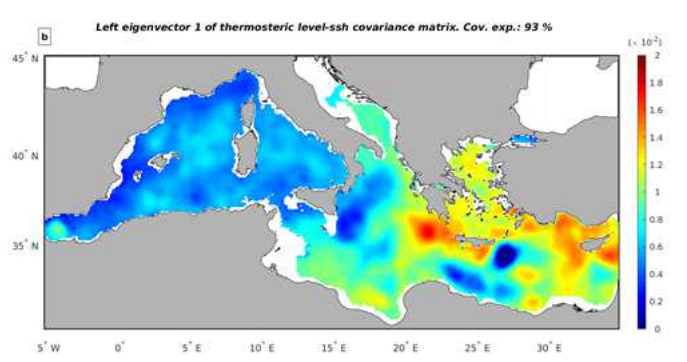

e
Original and CCM reconstructed PC1 of the NA salinity (E=12,τ=4). Corr. = 0.97
CCM recontructed
Original
← t[(E-1)·τ + 1] = 01-Sep-1996

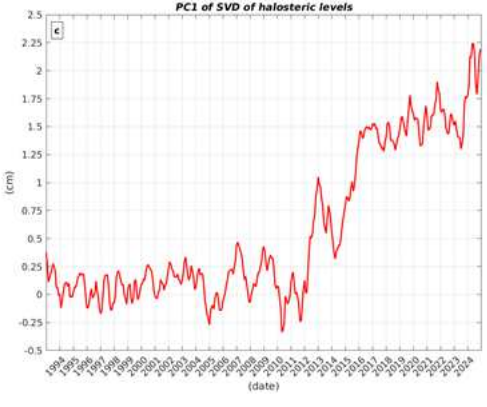

a
Right eigenvector of SPNA/Mediterranean SSS covariance. Covariance explained: 87 %
(× 10⁻²)
60° N
55° N
50° N
50° W
40° W
30° W
20° W
10° W

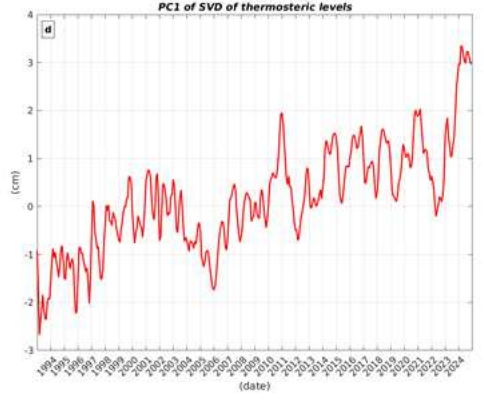

b
Left eigenvector of SPNA/Mediterranean SSS covariance. Covariance explained: 87 %
(× 10⁻²)
45° N
40° N
35° N
5° W
0°
5° E
10° E
15° E
20° E
25° E
30° E

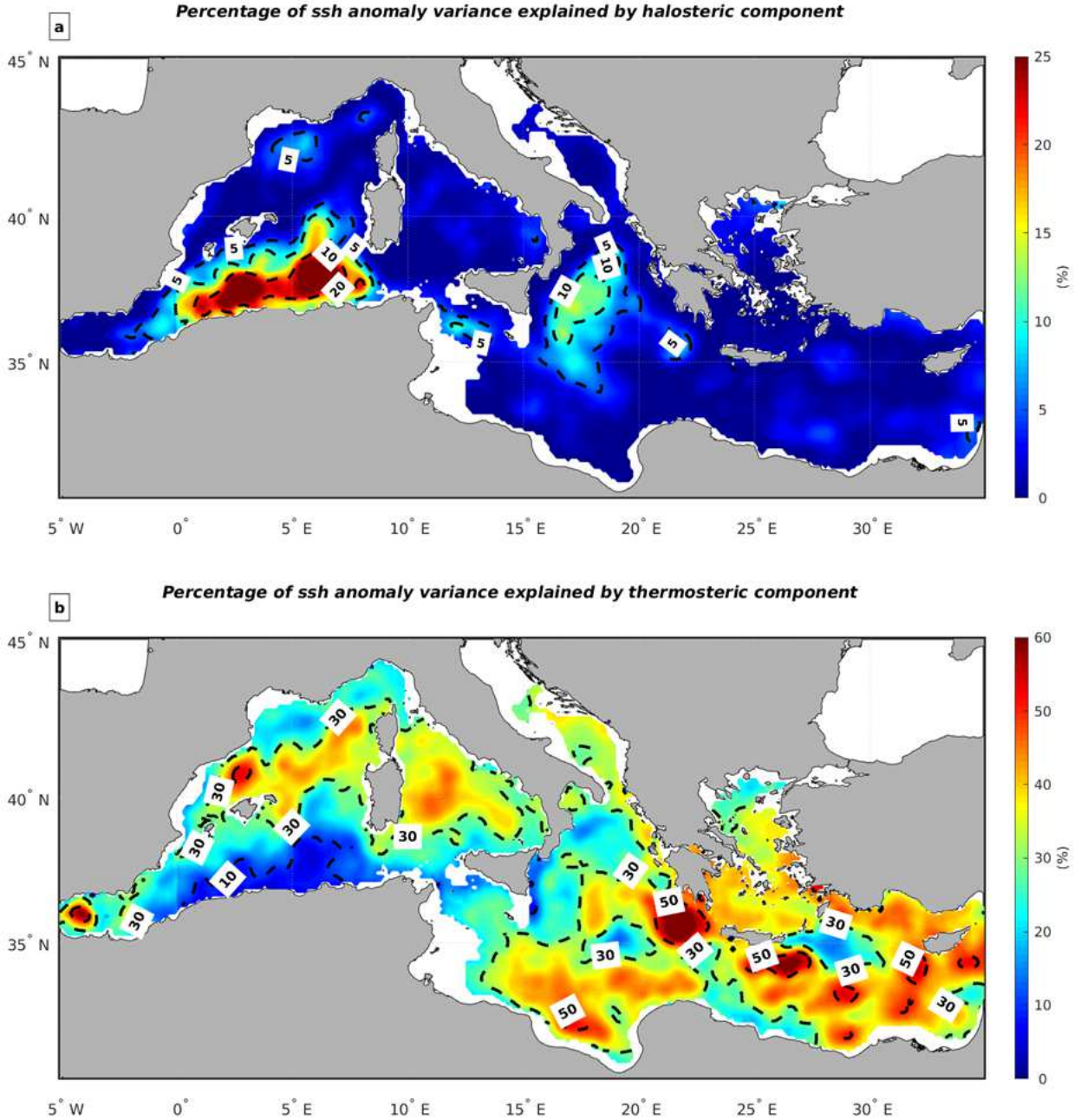

c
PC1 of SVD in the SPNA and Mediterranean
North Atlantic
Mediterranean
(psu)
(date)


a
Left eigenvector 1 of halosteric level-ssh covariance matrix. Cov. exp.: 93 %
(× 10^-2)
45° N
40° N
35° N
5° W
0°
5° E
10° E
15° E
20° E
25° E
30° E


b
Left eigenvector 1 of thermosteric level-ssh covariance matrix. Cov. exp.: 93 %
(× 10^-2)
45° N
40° N
35° N
5° W
0°
5° E
10° E
15° E
20° E
25° E
30° E


c
PC1 of SVD of halosteric levels
(cm)
(date)


d
PC1 of SVD of thermosteric levels
(cm)
(date)


a
Percentage of ssh anomaly variance explained by halosteric component
45° N
40° N
35° N
5° W
0°
5° E
10° E
15° E
20° E
25° E
30° E
(%)
b
Percentage of ssh anomaly variance explained by thermosteric component

Supplementary Files

This is a list of supplementary files associated with this preprint. Click to download.

- SupplementaryInfoFINALE.docx